SUPPLEMENT TO THE *WELDING JOURNAL*, MARCH 2015
Sponsored by the American Welding Society and the Welding Research Council

WELDING RESEARCH

Interfacial Microstructure of Laser Brazed AZ31B Magnesium to Sn-Plated Steel Sheet

Brazeability, interfacial microstructure, and mechanical properties were investigated

BY A. M. NASIRI, D. C. WECKMAN, AND Y. ZHOU

ABSTRACT

The brazeability of AZ31B-H24 magnesium alloy sheet to Sn-coated plain carbon steel sheet using a Mg-Al-Zn alloy filler metal and a diode laser heat source has been investigated. While the Sn coating promoted good wetting between the molten filler metal and the steel sheet, it did not play a role in forming the final metallic bond. Its primary function appeared to be in maintaining an oxide-free steel surface until the molten Mg filler metal could come in direct contact with the steel surface. In all cases, failure of transverse tensile shear test specimens of the joint occurred in the steel base metal. Metallic bonding between the magnesium alloy and the steel was facilitated by the formation of two transition layers, including a Fe(Al) solid solution formed on the surface of the steel and a nano-scale layer of $Al_8(Mn,Fe)_5$ phase on the Fe(Al) surface layer. Examination of the Fe(Al)-$Al_8(Mn,Fe)_5$ and $Al_8(Mn,Fe)_5$-Mg interfaces using HR-TEM showed that orientation relationships (OR) with a low angle of rotation of the matching planes and low interplanar mismatch and therefore low interfacial energy density existed at the Fe(Al) $Al_8(Mn,Fe)_5$ interface (i.e., when $[10\bar{1}1]_{Al8Mn5}$ //$[\bar{1}11]_{Fe(Al)}$, $\{110\}_{Fe(Al)}$ was 4.2 deg from $\{30\bar{3}3\}_{Al8Mn5}$ with 5.2% interplanar mismatch) and a high angle of rotation of the matching planes and large interplanar mismatch, and therefore, high interfacial energy density existed at the Al_8Mn_5-Mg interface (i.e., when $[10\bar{1}1]_{Al8Mn5}$//$[10\bar{1}0]_{Mg}$, $\{30\bar{3}3\}_{Al8Mn5}$ was within 47.4 deg of the $\{0002\}_{Mg}$ with 16.8% interplanar mismatch). These results were further validated using an edge-to-edge crystallographic matching model of the Fe(Al)-$Al_8(Mn,Fe)_5$ and $Al_8(Mn,Fe)_5$-Mg interfaces.

KEYWORDS

• Laser Brazing • AZ31B Mg sheet • Sn-Coated Steel Sheet • Electron Microscopy • Interfaces

Introduction

Automotive manufacturers are coming under increasing regulatory pressure to improve the overall fleet mileage of their automobiles. This has created a need to develop and assess new advanced materials and manufacturing technologies that will allow fabrication of lighter weight automotive bodies and structural components, thereby increasing fuel efficiencies and lowering environmental impact of vehicles. While magnesium alloys, with their combination of low density and high specific tensile strengths, could potentially be used to advantage to reduce the overall weight of a vehicle (Refs. 1, 2), sheet steels remain the most commonly used material in the automotive industry, due to their consistent properties, excellent ductility, and their lower material and fabrication costs (Ref. 3). Thus, the ability to make hybrid structures of magnesium alloy and steel sheet would facilitate the increased use of magnesium alloys and light-weighting of automotive structures. This will require the development of new techniques and processes that can be used to make reliable and low cost dissimilar metal joints between magnesium alloy and steel sheet (Refs. 4–11).

It is difficult to join magnesium alloys directly to steel by conventional fusion welding technologies due to the large difference in their melting temperatures and the nearly zero solubility of magnesium and iron (Ref. 4). The melting point of steel (≈ 1823 K [1550ºC]) is well above the boiling point of magnesium (1380 K [1107ºC]), and this can cause catastrophic vaporization of the molten magnesium during a fusion welding process. In addition, the maximum solid solubility of Fe in Mg is only 0.00041 at.-% Fe (Ref. 4). There is also clear evidence that magnesium and steel do not react with each other and do not mix in the liquid state at ambient pressure (Ref. 4). Thus, metallurgical bonding between these two metals

A. M. NASIRI (amnasiri@uwaterloo.ca), D. C. WECKMAN, and Y. ZHOU are with Department of Mechanical & Mechatronics Engineering, Center for Advanced Materials Joining, University of Waterloo, Waterloo, Ont., Canada.
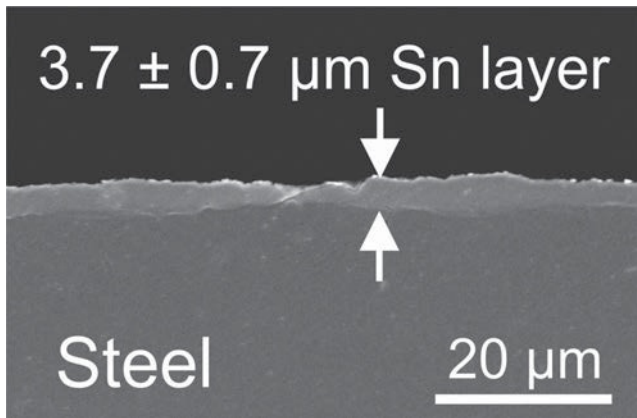
Fig. 1 — Transverse section of the Sn electroplated layer on the steel substrate.
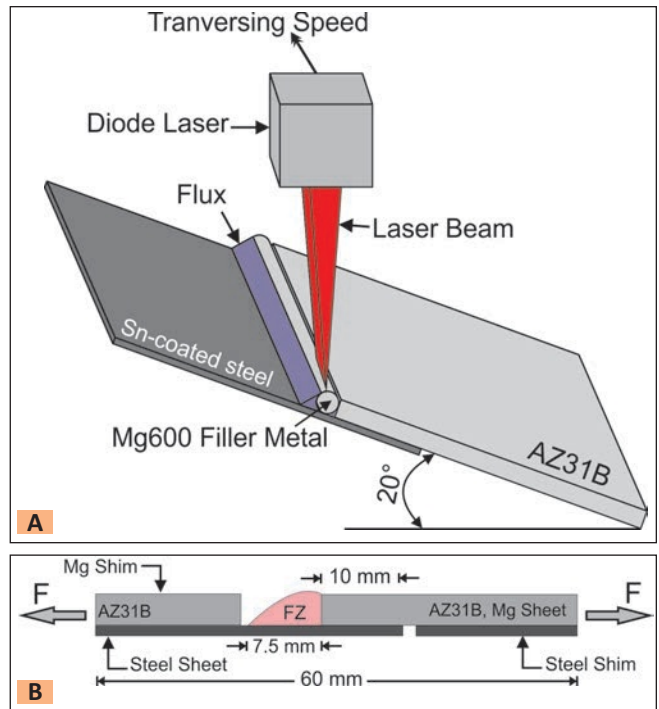

Fig. 2 — A — Schematic of the laser brazing system used for joining AZ31B Mg and Sn electroplated steel sheets in the lap joint configuration; B — schematic of the 10-mm-wide tensile shear test specimen.

will only be possible provided another element that can interact and bond with both of them can be applied between the Mg and Fe and act as an intermediate interlayer element or alloy.

The weldability of magnesium to steel using various processes such as hybrid laser-arc welding (Refs. 4, 7, 9, 11), resistance spot welding (RSW) (Ref. 10) and friction stir welding (FSW) (Refs. 12, 13) have been examined. In addition, the benefits of using various interlayer alloys and elements such as Al-12Si (Ref. 14), Ni (Refs. 7, 15), Cu (Refs. 7, 11), and Zn (Refs. 8, 10, 16–18) have been explored. In more recent studies, the feasibility of using the laser brazing or laser weld-brazing processes in conjunction with different interlayers have been explored (Refs. 14–18). The laser-brazing process combines attributes of furnace brazing and laser welding (Ref. 19). Also, laser brazing and laser welding-brazing can prevent or minimize excessive formation of detrimental brittle intermetallic phases (Ref. 20). However, if intermetallic layers can be limited to thicknesses below 10 μm, then acceptable joint strengths and mechanical properties may be realized (Refs. 5, 21).

In previous studies (Refs. 14, 15), a diode laser brazing process was developed for joining Mg alloy sheet to coated steel sheet where the Al-12Si and Ni coatings served as the interlayers. These coatings were found to promote wetting of the steel by the magnesium brazing alloy; however, in the case of the Al-12Si coating layer, a preexisting layer of brittle θ-FeAl$_3$ along the braze-steel interface was found to degrade the mechanical properties of the joint. Nasiri et al. (Ref. 15) also showed that improved wetting and bonding between the magnesium brazing alloy and electroplated Ni steel sheet was facilitated by the formation of an Fe(Ni) solid solution on the steel surface. The average fracture shear strength of the metallic bond reached 96.8 MPa and the joint efficiency was 60% with respect to the AZ31B-H24 Mg alloy base metal. Clearly, selection of an appropriate interlayer for joining Mg to steel depends on identification of an interlayer composition that promotes both good wetting and bonding between the brazing alloy and the steel without generating layers of brittle inter-

metallics or other reaction products at the joint interface that limit the joint strength.

Following a review of binary and ternary phase diagrams, Sn was identified as a potentially viable interlayer element between the steel and the Mg-Al-Zn brazing alloy used in our previous studies (Refs. 14, 15). Therefore, the objectives of the present study were to investigate the brazeability, interfacial microstructure, and mechanical properties of the laser brazed AZ31B-H24 magnesium alloy to steel sheet with a layer of Sn on the steel to act as the interlayer element. It is expected that development of this laser brazing technology for joining of steel-interlayer-Mg alloy combinations with a strong metallurgical bond between the steel and Mg alloy will facilitate increased application and use of Mg alloys in the automotive industry.

Table 1 — Measured Chemical Composition of the AZ31-H24 Mg Alloy Sheet and TiBraze Mg 600 Filler Metal (wt-%)

	Al	Zn	Mn	Si	Mg
AZ31B-H24	3.02	0.80	0.30	0.01	Bal.
TiBraze Mg 600	9.05	1.80	0.18	—	Bal.

Table 2 — Measured Chemical Composition of the 0.6-mm-Thick Steel Sheet (wt-%)

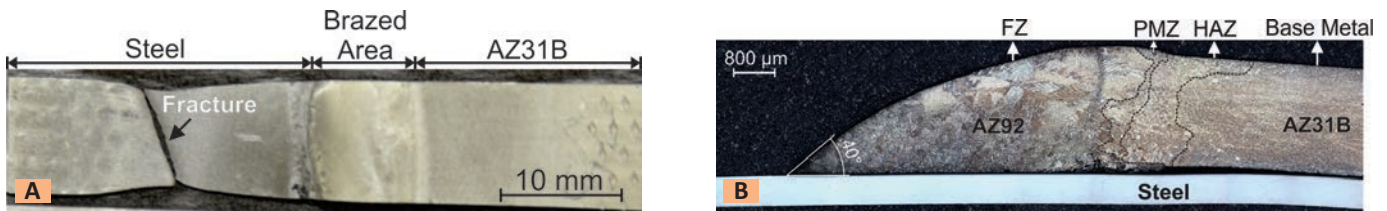| C	Mn	P	S	Fe
0.01	0.5	0.010	0.005	Bal.

Fig. 3 — A — A typical fractured specimen after tensile shear test of the laser brazed joint; B — transverse section of a laser brazed Sn electroplated steel/AZ31B joint made using 2.2-kW laser power, 8 mm/s travel speed, and 0.2-mm beam offset to the steel side.
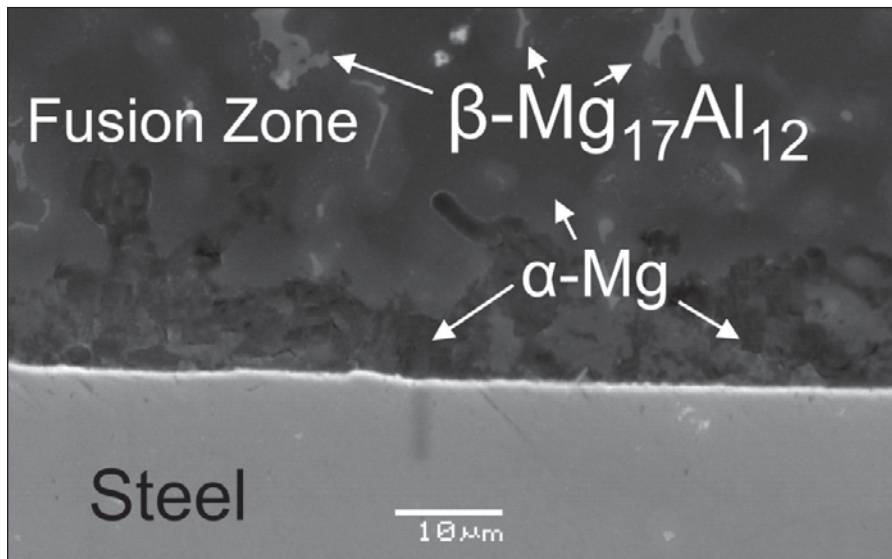

Fig. 4 — SEM image along the steel-FZ interface.

Experimental Apparatus and Procedures

The laser brazing process was carried out on 60 × 50-mm specimens sheared from 2-mm-thick, commercial-grade, twin-roll strip cast AZ31B-H24 Mg alloy sheet and 0.6-mm-thick Sn-coated, cold-rolled AISI 1008 plain carbon steel sheet in a lap joint configuration. The electroplated Sn coating layer on the steel sheet was 3.7 ± 0.7 μm thick. Figure 1 shows a SEM micrograph of the cross section of the Sn electroplated steel. The brighter layer on top of the steel is the Sn coating layer. The coating was of uniform thickness with a void-free interface. EDS analysis of the Sn layer on the steel showed a pure Sn coating layer. The chemical compositions of the base materials are given in Tables 1 and 2. A 2.4-mm-diameter TiBraze Mg 600 filler metal (Mg-Al-Zn alloy) with solidus and liquidus temperatures of 445° and 600°C, respectively, was chosen for this study. The commercial flux used in the experiments was Superior No. 21 manufactured by Superior Flux and Manufacturing Co. This powder flux was composed of LiCl (35–40 wt-%), KCl (30–35 wt-%), NaF (10–25 wt-%), NaCl (8–13 wt-%), and $ZnCl_2$ (6–10 wt-%) (Ref. 22).

Prior to laser brazing, the oxide layers on the surfaces of the magnesium sheets were cleaned by stainless steel wire brushing. All of the specimens were ultrasonically cleaned in acetone to remove oil and other contaminants from the specimen surfaces. The AZ31B sheet was then clamped on top of the steel sheet to make a lap joint configuration as shown in Fig. 2A. The filler metal was cut and set along the joint line with flux before heating and brazing by the laser beam.

An integrated Panasonic 6-axis robot and Nuvonyx diode laser system with a maximum power of 4.0 kW and a 0.5 × 12-mm rectangular laser beam intensity profile at the focal point were used for laser brazing. This energy distribution is more suitable for brazing processes compared with the nonuniform Gaussian-distributed circular beams generated by CO_2 and Nd:YAG lasers (Ref. 23). The beam was focused on top of the filler metal. Helium shielding gas was provided in front of the molten pool at a flow rate of 30 L/min from a 6-mm-diameter soft copper feeding tube. Laser brazing was performed using a range of laser powers, travel speeds and beam offset positions.

After laser brazing, 10-mm-wide rectangular-shaped specimens were cut from the brazed joints and subjected to tensile-shear tests with a crosshead speed of 1 mm/min. As shown in Fig. 2B, shims were used at each end of the specimens to ensure shear loads in the lap joint while minimizing induced couples or bending of the specimens.

Transverse sections of the brazed specimens were cut and mounted in epoxy resin. The samples were then mechanically ground using 300, 600, 800, 1000, and 1200 grades of SiC grinding papers followed by polishing using a 1-μm diamond suspension. The polished specimens were etched to reveal the microstructure of the braze metal and AZ31B base material. The etchant was comprised of 20 mL acetic acid, 3 g picric acid, 50 mL ethanol, and 20 mL water (Ref. 24). Macro- and microstructures of the etched joints were examined using an optical metallographic microscope. The microstructure and composition of different zones of the joint cross section were determined using a JEOL JSM-6460 SEM equipped with an Oxford INCA energy dispersive X-ray spectrometer (EDS). A TEM foil of the steel-fusion zone interfacial region was also prepared using a focused ion beam (FIB) and in-situ lift out technique. After attaching the TEM foil to a copper grid, final Ga-ion beam thinning was performed on the sample using an acceleration voltage of 30 kV,
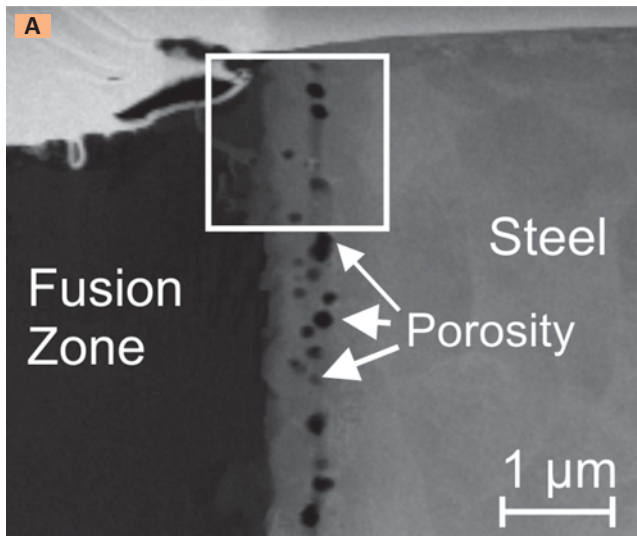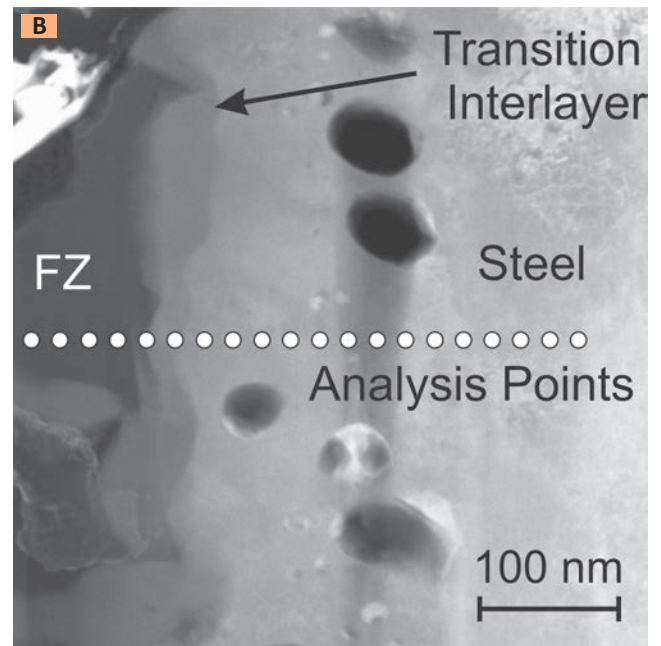
Fig. 5 — A — STEM image of the steel-fusion zone interface; B — higher magnification of the selected square area in A.

followed by 10 kV, and 1 kV for the final polishing step to get a 100-nm-thick TEM sample. The TEM studies were performed with a Titan 80-300LB, a high-resolution transmission electron microscope (HR-TEM) made by FEI Company.

Results

Visually acceptable laser brazed joints were made using 2.2-kW laser power, 8 mm/s travel speed, and 0.2 mm beam offset to the steel side. These conditions resulted in melting of the filler metal to form a fillet with triangular cross section between the AZ31B Mg and steel base metals — Fig. 3. There was a uniform brazed area with good wetting of the Mg-Al-Zn brazing alloy to the steel base metal and some melting of the AZ31B base metal. The average leg length of the Mg-Al-Zn alloy filler metal-steel interface was 7.5 ± 2.1 mm.

Figure 3A shows a typical tensile shear test of a laser-brazed specimen. All tensile-shear specimens fractured in the steel base metal well away from the brazed joint. The average fracture load of 10-mm-wide tensile shear specimens was found to be 2064 ± 85 N. This value was exactly the same as fracture load of the steel base metal with the same size tensile specimen, confirming that fracture of the laser brazed joint always occurred in the steel base metal. With an average interface area between the

braze alloy and the steel sheet was 75 mm^2; therefore, the tensile shear strength of the interface was greater than 2064/75 = 27.5 MPa.

A cross-sectional view of a typical laser brazed specimen is shown in Fig. 3B. The average contact angle of the fusion zone (FZ) on the steel substrate was measured to be 35 ±5 deg, which is indicative of good wetting of the Sn-coated steel substrate by the molten Mg filler metal (Ref. 25). Defects such as porosity or cracks were not observed in the joint. In contrast, when bare steel was used, no metallic bonding occurred between the steel sheet and the braze alloy (fusion zone) and wetting of the steel by the braze metal was very poor (Ref. 14).

Microstructural Analysis of the Steel-FZ Interface

The microstructure in the AZ31B-H24 Mg base metal and filler metal were similar to that observed in previous studies with these alloys (Refs. 14, 15). As indicated in Fig. 3B, in the base metal, continued recrystallization and grain growth occurred in the AZ31B heat-affected zone (HAZ). In the partially melted zone (PMZ), localized melting or liquation of the intergranular regions occurred. The solidification microstructure of the FZ was a combination of columnar and equiaxed α-Mg dendrites with a divorced eutectic β-$Mg_{17}Al_{12}$ intermetallic phase at the

dendrite boundaries. A more detailed microstructural analysis of the fusion zone and AZ31B Mg alloy microstructure may be found in Ref. 14.

Figure 4 shows a typical SEM image of the microstructure along the steel-fusion zone interface. After the laser brazing process, the Sn coating was not detected as a separate layer along the interface. This suggests that the low melting point Sn (T_{mp} = 505 K [232 ºC]) layer had been entirely melted and mixed with the molten Mg filler metal immediately adjacent to the interface. The microstructure of the steel-FZ interface was the same along the entire length of the interface. The contrast of α-Mg adjacent to the interface looks darker than the α-Mg in the fusion zone, meaning lower Al content of α-Mg adjacent to the interface — Fig. 4. Therefore, Al atoms near the interface should be consumed in a way, which is unclear according to the SEM photomicrograph. While this SEM photomicrograph might suggest that the α-Mg phase has bonded directly to the steel substrate, it is well known that this will not occur due to the very large lattice mismatching of Fe and Mg (Refs. 4, 5). In our previous studies (Refs. 14, 15), a submicron-thick transitional layer or phase was found to exist at the steel-magnesium interface that could not be resolved by optical microscopy or the SEM. This intermediate phase was found through TEM examination to be responsible
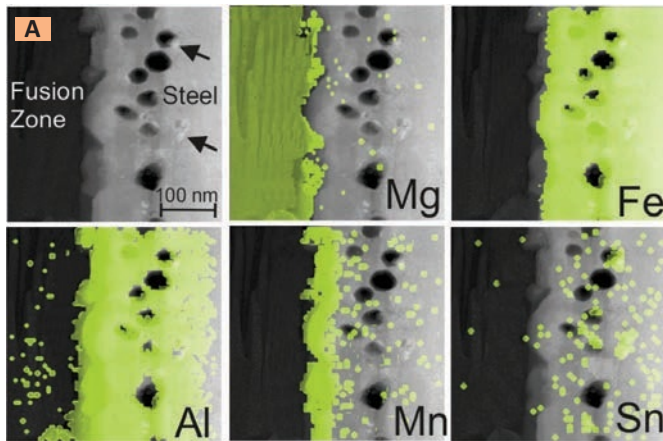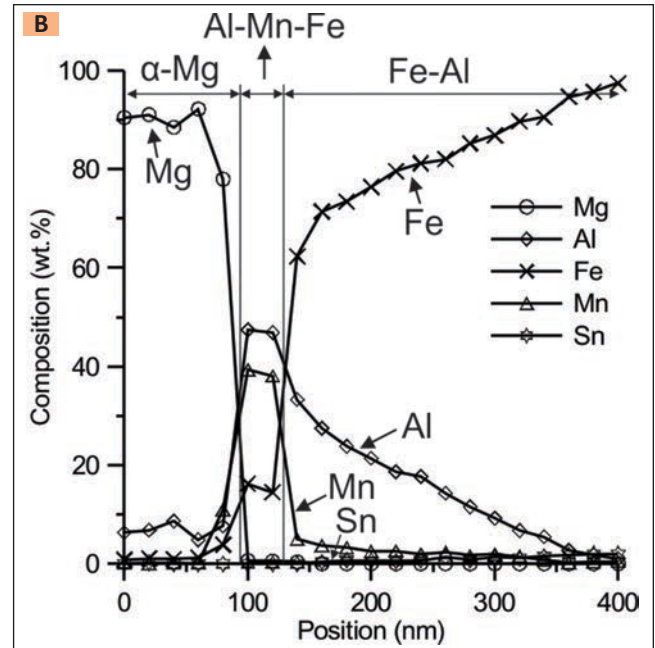
Fig. 6 — A — STEM-EDS concentration maps; B — STEM-EDS composition line scans across the steel-fusion zone interface shown in Fig. 5B, indicating scans of Mg, Fe, Al, Mn, and Sn.

for the metallurgical bond between these two immiscible alloys.

Figure 5A shows a scanning transmission electron microscopy (STEM) image of the steel-fusion interface. Complete metallurgical bonding appears to have occurred along the entire length of the interface; however, there is a band of nanoscale pores with an average diameter of 145 ± 22 nm in the steel substrate adjacent to the interface. As shown at even higher magnification in Fig. 5B, a very thin layer of a distinctly different phase exists between the steel and the fusion zone, which appears to have created a transitional interlayer between these two alloys that forms a bond with the steel substrate on one side as well as the magnesium filler alloy on the other side.

STEM-EDS compositional mapping and point scan analysis were used to identify the composition of the phases formed at the steel-fusion zone interface shown in Fig. 5. Figure 6A shows a STEM image of a representative area of the interface and concentration maps of this same area for Mg, Fe, Al, Mn, and Sn. Mg is seen to be present primarily in the fusion zone, but nowhere else. Similarly, Fe from the steel exists up to the interlayer, but is not present in the fusion zone. The nanoscale pores are within the Fe. There is a significant concentration of Al from the braze alloy within the interlayer and also to a depth of about 270 nm into the steel substrate and past the band of pores. Mn, also from the braze alloy, is concentrated primarily within the interlayer and is not de-

tected in significant quantities elsewhere in the braze alloy and only in small concentrations in the steel. Finally, there appears to be very low concentrations of Sn only within the steel close to the interface.

The composition and distribution of elements across the interface between the steel and fusion zone was also analyzed using STEM-EDS point analysis along the line shown in Fig. 5B. These results are shown in Fig. 6B and are consistent with those shown in the element maps in Fig. 6A, e.g., the Mg exists only in the filler metal and Sn is detectable in only very small concentrations within the steel. While the Al concentration in the fusion zone is close to the nominal 9 wt-% Al of the braze alloy (Fig. 6B and Table 1), the concentration increases in a stepwise fashion to about 48 wt-% Al in the interlayer and then drops to about 31 wt-% followed by a continual decrease of the Al concentration to a distance of about 270 ± 46 nm into the steel, which is past the band of pores. This is indicative of solid-state diffusion of the Al into the steel. With the increased Al concentration in the steel, there is a complementary decrease of the Fe concentration at the steel surface approaching the interlayer. The Fe concentration appears to drop to about 15 wt-% in the interlayer and is not detected in the fusion zone. Mn, also present in concentrations less than 1 wt-% in all three alloys, is concentrated up to 40 wt-% primarily within the interlayer and is not de-

tected in significant quantities elsewhere in the braze alloy and only in small concentrations in the steel. The average thickness of the interlayer was 45 ± 10 nm and it contained only 60.9 ± 0.2 at.-% Al, 34.8 ± 0.6 at.-% Mn, and 4.3 ± 0.4 at.-% Fe. This suggests that the interlayer is composed of the $Al_8(Mn,Fe)_5$ intermetallic compound.

The range of composition in the Fe-Al diffusion layer evident in Fig. 6B is consistent with the range of Al composition over which the disordered α-Fe and ordered Fe-Al solid solution phases exist in the Fe-Al binary phase diagram (Ref. 26). This was confirmed using selected area diffraction pattern analysis (SADP). Figure 7A shows a bright field TEM image of the interface region between the steel substrate, the $Al_8(Mn,Fe)_5$ interlayer and the Mg braze alloy and Fig. 7B shows a SADP obtained from the Fe-Al phase region. Analysis of this pattern indicated that this phase is a Fe(Al) solid solution with a body-centered cubic (BCC) crystal structure. The SADP was taken along the $[\bar{1}11]$ zone axis of the phase. The lattice parameter of Fe(Al) was calculated to be $a = 2.885$ Å, which is similar to the lattice parameter of Fe ($a_{Fe} = 2.8606$ Å). Thus, the crystal structure and the lattice parameter of Fe(Al) were similar to Fe. The Fe-Al binary phase diagram shows up to 55 at.-% solid solubility for Al in Fe (Refs. 26, 27). The Fe(Al) is well-known for its relatively high strength, high oxida-
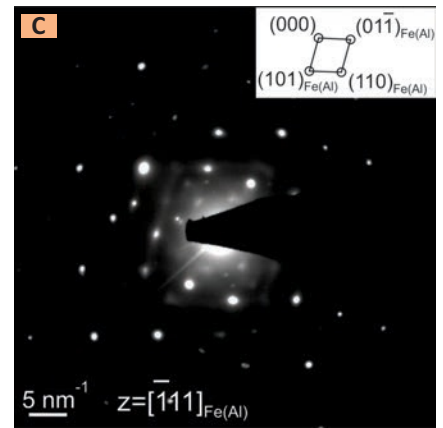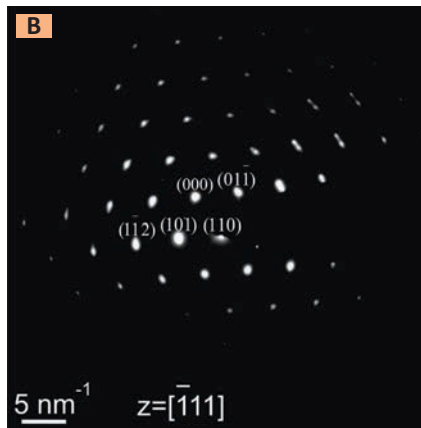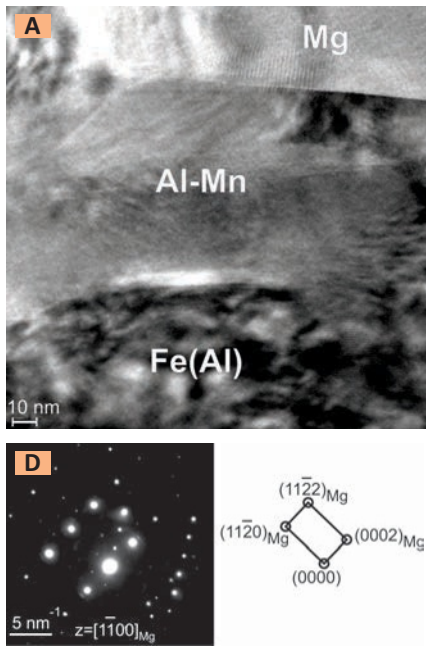
Fig. 7 — A — Bright field TEM image of the Fe(Al)/Al-Mn/Mg (substrate-fusion zone) interfaces; B — a SADP of the Fe(Al) phase in the [111] zone axis of this phase; C — a SADP analysis of the Fe(Al)-Al_8Mn_5 interface; D — a SADP analysis of the Al_8Mn_5-Mg interface, schematic is showing the indexed SADP of the Mg along [1$\bar{1}$00] zone axis of the Mg.

tion resistance, low cost, and excellent fracture toughness (Refs. 18, 28). Figure 7C shows a SADP analysis of the Fe(Al)-Al_8Mn_5 interface, where the lattice of Fe(Al) was exactly located on the [$\bar{1}$11] zone axis of the phase. The diffraction spots from the Fe(Al) were indexed accordingly. The extra spots in Fig. 7C are from the Al_8Mn_5 phase. This figure shows that while the Fe(Al) is in the [$\bar{1}$11] zone axis orientation, the Al_8Mn_5 intermetallic compound is off any low index orientation.

According to the results of thermodynamic calculations under Scheil cooling conditions performed by Kim et al. (Ref. 29), during solidification of the Mg-Al-Zn brazing alloy, the sequence of phase formation during solidification is first Al_8Mn_5, then α-Mg and finally the β-phase ($Mg_{17}Al_{12}$). Therefore, it is expected in the present study that a thin layer of Fe(Al) at the steel-FZ interface forms first by solid-state diffusion of Al in the FZ liquid into the steel. Upon further cooling, the Al_8Mn_5 intermetallic nucleates and grows on the Fe(Al) surface layer that has formed on the steel and there is time for a thin layer to grow and cover the Fe(Al) (BCC) surface. Thereafter, the remaining FZ liquid will be in contact with only the thin Al_8Mn_5 layer and this new interlayer phase now plays the role of the substrate for subsequent reactive wetting, nucle-

ation and growth of the remaining α-Mg liquid onto the thin surface layer of Al_8Mn_5. A SADP analysis of the Al_8Mn_5-Mg interface is shown in Fig. 7D. When the Mg phase was parallel to the [1$\bar{1}$00] zone axis, again the Al_8Mn_5 phase was off any low indexed orientation.

Measurements of the Crystallographic Orientation Relationships at the Steel-FZ Interface

When reaction products form at the interface of dissimilar metals, the bond strength between the two phases is directly affected by the interfacial energy density of the interface, which in turn depends on the degree of crystallographic registry, i.e., the crystallographic orientation relationship (OR) and lattice matching, that exists between the two phases at their interface (Refs. 25, 30). In the present study, in order to identify the OR and lattice matching between the Al_8Mn_5 phase with a rhombohedral crystal structure and the BCC Fe(Al) phase on the one side (steel) and the hexagonal close-packed (HCP) α-Mg phase on the other side (fusion zone), high-resolution (HR)-TEM analysis of the interface was performed.

Figure 8A shows a HR-TEM image of the Al_8Mn_5 phase-Fe(Al) substrate interface. When the specimen was aligned with the direction of Al_8Mn_5

[10$\bar{1}$1], the {110}$_{FeAl}$ was within 4.2 deg of the {30$\bar{3}$3}$_{Al8Mn5}$ and the measured interplanar spacing for these planes were $d_{\{110\}FeAl}$ = 2.095 Å and $d_{\{30\bar{3}3\}Al8Mn5}$ = 2.204 Å, which represents only 5.2% interplanar mismatch at the interface. Thus, good lattice matching with low angle rotation of matched lattice planes exists between the Fe(Al) and Al_8Mn_5 phases at this interface. This good match of lattice sites between Al_8Mn_5 and Fe(Al) leads to a low energy density at their interface.

Figure 8B shows the HR-TEM image of the Al_8Mn_5-α-Mg interface. Using HR-TEM, it was found that when [10$\bar{1}$1]$_{Al8Mn5}$//[10$\bar{1}$0]$_{Mg}$, the {30$\bar{3}$3}$_{Al8Mn5}$ was within 47.4 deg of the {0002}$_{Mg}$. Similarly, the measured d-value for the {0002}$_{Mg}$ was 2.574 Å. This represents 16.8% mismatch with that of the {30$\bar{3}$3}$_{Al8Mn5}$. This analysis showed a poor crystallographic matching between Al_8Mn_5 and α-Mg with a large angle rotation of matching planes and therefore high energy density at their interface.

Discussion

Analysis of the Interface Orientation Relationships at the Steel-FZ Interface

The HR-TEM measurements indicated that good OR and lattice match-
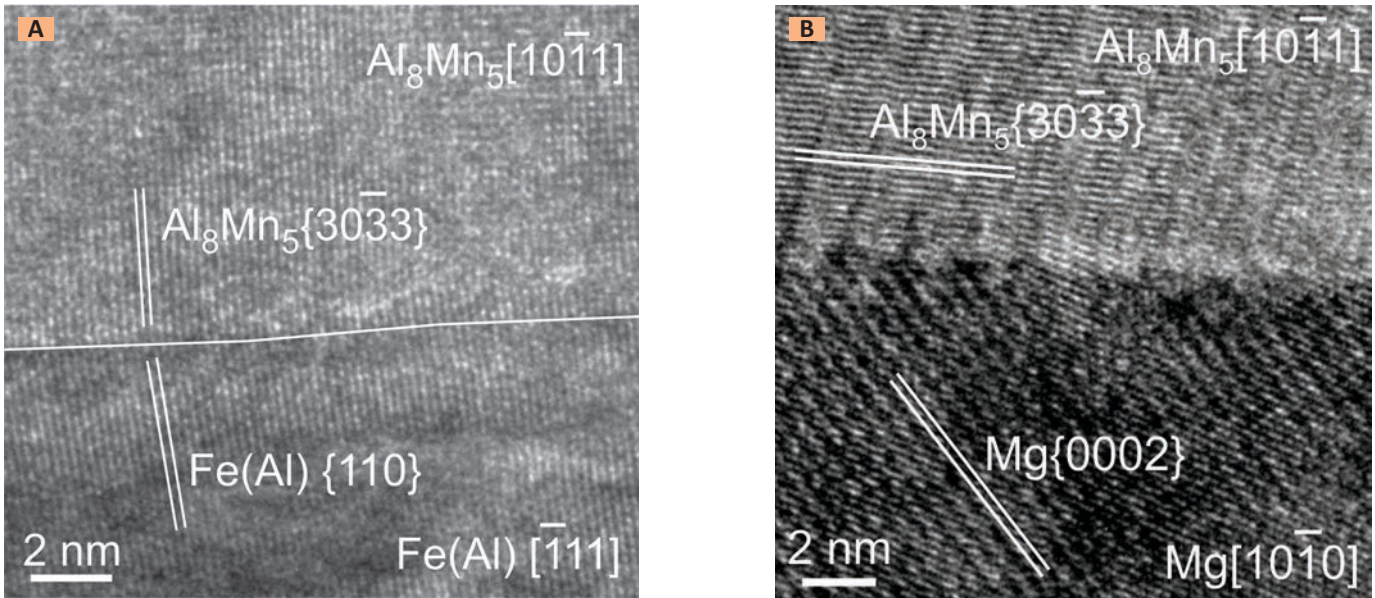
Fig. 8 — HR-TEM image of A — Fe(Al)–Al$_8$Mn$_5$ interface; B — Al$_8$Mn$_5$–Mg interface.

ing exists between the Al$_8$Mn$_5$ and Fe(Al) phase on the steel side and poor crystallographic matching was found between the Mg and the Al$_8$Mn$_5$ layer on the Mg-Al-Zn brazing alloy side. However, the observed ORs were more like a local observation at the interface than a general trend of OR. Therefore, further analysis of the possible formed ORs at the interface is required. Due to different lattice parameters between Al$_8$Mn$_5$, Fe(Al) and Mg, an intrinsic strain in their adjoining lattices arises. If this strain is not relaxed by the introduction of misfit dislocations, the magnitude of this extensional strain will be proportional to the lattice mismatch between Al$_8$Mn$_5$ and Fe(Al) from one side and Mg from the other side (Ref. 31). This strain will increase the total interfacial energy. As a result, the strength of the formed interfaces decreases. In such a way, the interfacial energy and metallic bond strength can be dependent on the crystallographic disregistry and lattice matching along Fe(Al)-Al$_8$Mn$_5$-Mg adjoining lattices. In addition, the effectiveness of a substrate in promoting heterogeneous nucleation, such as Fe(Al) for Al$_8$Mn$_5$ or Al$_8$Mn$_5$ for Mg, depends on the crystallographic OR and lattice matching between the substrate and the solidified region (Ref. 32). To further study possible formed ORs along the Fe(Al)-Al$_8$Mn$_5$ and Al$_8$Mn$_5$-Mg interfaces, the edge-to-

edge crystallographic model developed by Zhang and Kelly (Refs. 33, 34) was used. The model is based on the assumptions that crystallographic relationships between any two phases can be obtained by minimization of the strain energy density of the interface and that the necessary and sufficient condition for minimization of the strain energy is the matching of rows of atoms in the two phases (Ref. 33).

Using the edge-to-edge matching model, the interatomic spacing misfits along matching directions and mismatches between matching planes can be calculated. It is assumed that the matching directions and matching planes are the close or nearly close-packed directions and planes (Refs. 33, 34). The interatomic misfit and interplanar mismatch between two phases can be calculated by:

$$\delta = \frac{|\Delta a_0|}{a_0}$$

$$(1)$$

where Δa_0 is the difference between interatomic or interplanar spacings of the two phases and a_0 is the interatomic or interplanar spacing of the substrate for a specific direction or plane (Ref. 34). According to the edge-to-edge model (Ref. 34), in order to predict the OR between Fe(Al) with BCC crystal structure and Al$_8$Mn$_5$ with rhombohedral structure, the close-

packed or nearly close-packed directions must first be identified.

Al$_8$(Mn,Fe)$_5$ is a substitutional solid solution of Al$_8$Mn$_5$, in which some Mn atoms are replaced by Fe. Solution of the Fe atoms into Al$_8$Mn$_5$ and replacement of the Mn atoms by Fe atoms do not cause significant variation in the lattice parameters, since the atomic radius of Mn and Fe are very close (0.112 and 0.124 nm, respectively). Therefore, Al$_8$(Mn,Fe)$_5$ can be treated as Al$_8$Mn$_5$ with Al$_8$Cr$_5$ type of rhombohedral structure. In this case, the lattice parameters for Al$_8$Mn$_5$ are α = 1.2645 nm and c = 1.5855 nm (Ref. 35).

The unit cell of Al$_8$Mn$_5$ (or Al$_8$(Mn,Fe)$_5$ contains 48 Al atoms and 30 Mn/Fe atoms. From these atoms' positions in the unit cell of Al$_8$Mn$_5$ together with the X-ray diffraction intensity data (Ref. 36), the close-packed or nearly close-packed planes of Al$_8$(Mn,Fe)$_5$ were identified to be $\{30\bar{3}3\}_{Al8Mn5}$ and $\{33\bar{6}0\}_{Al8Mn5}$. Similarly, the close-packed or nearly close-packed directions are $\langle11\bar{2}0\rangle_{Al8Mn5}$, $\langle0001\rangle_{Al8Mn5}$, $\langle1\bar{1}02\rangle_{Al8Mn5}$, and $\langle10\bar{1}1\rangle_{Al8Mn5}$.

The lattice parameters of Fe(Al) used in this study was $a_{Fe(Al)}$ = 0.2885 nm (measured from the SADP of the Fe(Al) phase in Fig. 8B). In the BCC crystal structure, there are four possible close-packed or nearly close-packed
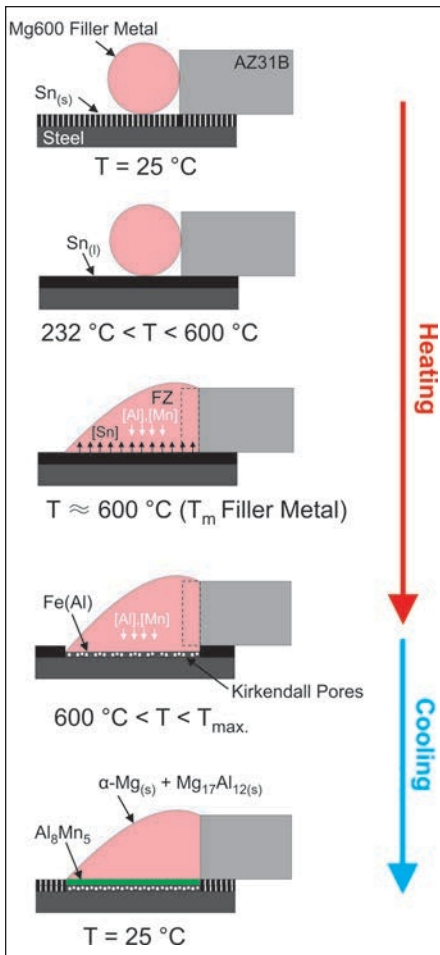
Fig. 9 — Schematic of interfacial layers formation during the laser brazing of Sn electroplated steel-AZ31B with Mg alloy filler metal: A — Lab joint design configuration prior to the laser brazing process at room temperature; B — melting of Sn electroplated layer during heating; C — melting of the filler metal and dissolution of liquid Sn into the FZ; D — formation of Fe(Al) phase containing Kirkendall porosities on top of the steel substrate; E — nucleation of Al_8Mn_5 IMC on top of Fe(Al) phase and solidification of the FZ during cooling.

three close-packed or nearly close-packed planes, i.e., $\{110\}_{Fe(Al)}$, $\{200\}_{Fe(Al)}$, and $\{111\}_{Fe(Al)}$. Thus, there are a total of six possible plane pairs between Fe(Al) (BCC) and Al_8Mn_5 (rhombohedral) that are potential matching planes. For the BCC crystal structure, the interplanar spacing, d, between adjacent $\{110\}_{Fe(Al)}$, $\{200\}_{Fe(Al)}$, and $\{111\}_{Fe(Al)}$ planes are

$$\frac{\sqrt{2}}{2}a_{Fe(Al)}, \ 0.5a_{Fe(Al)}, \ \text{and} \ \frac{\sqrt{3}}{3}a_{Fe(Al)}, \ \text{re-}$$

spectively. Table 4 shows the calculated interplanar spacings for the

Al_8Mn_5 phase and the Fe(Al) substrate as well as the interplanar spacing mismatches.

According to the data shown in Table 3, the matching directions with interatomic spacing misfits less than the critical value of 10% between the Fe(Al) substrate and Al_8Mn_5 phase at the interface are: $\langle 111 \rangle_{Fe(Al)}//\langle 11\bar{2}0 \rangle_{Al8Mn5}$, $\langle 111 \rangle_{Fe(Al)}//\langle 10\bar{1}1 \rangle_{Al8Mn5}$, $\langle 100 \rangle_{Fe(Al)}//\langle 1\bar{1}02 \rangle_{Al8Mn5}$, $\langle 100 \rangle_{Fe(Al)}//\langle 10\bar{1}1 \rangle_{Al8Mn5}$, $\langle 110 \rangle_{Fe(Al)}//\langle 0001 \rangle_{Al8Mn5}$, and $\langle 113 \rangle_{Fe(Al)}//\langle 11\bar{2}0 \rangle_{Al8Mn5}$. The selection

Table 3 — Interatomic Spacing Misfits along Possible Matching Directions between Al_8Mn_5 Phase and Fe (Al) Substrate

Matching Directions	Fe(Al) Interatomic Spacing, nm	Al_8Mn_5 Interatomic Spacing, nm	Interatomic Misfit (%)
$\langle 111 \rangle_{Fe(Al)}//\langle 11\bar{2}0 \rangle_{Al8Mn5}$	0.250	0.244	2.4
$\langle 111 \rangle_{Fe(Al)}//\langle 1\bar{1}02 \rangle_{Al8Mn5}$	0.250	0.289	15.6
$\langle 111 \rangle_{Fe(Al)}//\langle 0001 \rangle_{Al8Mn5}$	0.250	0.401	60.4
$\langle 111 \rangle_{Fe(Al)}//\langle 10\bar{1}1 \rangle_{Al8Mn5}$	0.250	0.264	3.3
$\langle 100 \rangle_{Fe(Al)}//\langle 11\bar{2}0 \rangle_{Al8Mn5}$	0.288	0.244	15.3
$\langle 100 \rangle_{Fe(Al)}//\langle 1\bar{1}02 \rangle_{Al8Mn5}$	0.288	0.289	0.3
$\langle 100 \rangle_{Fe(Al)}//\langle 0001 \rangle_{Al8Mn5}$	0.288	0.401	39.2
$\langle 100 \rangle_{Fe(Al)}//\langle 10\bar{1}1 \rangle_{Al8Mn5}$	0.288	0.264	8.3
$\langle 110 \rangle_{Fe(Al)}//\langle 11\bar{2}0 \rangle_{Al8Mn5}$	0.408	0.244	40.2
$\langle 110 \rangle_{Fe(Al)}//\langle 1\bar{1}02 \rangle_{Al8Mn5}$	0.408	0.289	29.2
$\langle 110 \rangle_{Fe(Al)}//\langle 0001 \rangle_{Al8Mn5}$	0.408	0.401	1.7
$\langle 110 \rangle_{Fe(Al)}//\langle 10\bar{1}1 \rangle_{Al8Mn5}$	0.408	0.264	35.3
$\langle 113 \rangle_{Fe(Al)}//\langle 11\bar{2}0 \rangle_{Al8Mn5}$	0.239	0.244	2.1
$\langle 113 \rangle_{Fe(Al)}//\langle 1\bar{1}02 \rangle_{Al8Mn5}$	0.239	0.289	20.9
$\langle 113 \rangle_{Fe(Al)}//\langle 1001 \rangle_{Al8Mn5}$	0.239	0.401	67.8
$\langle 113 \rangle_{Fe(Al)}//\langle 10\bar{1}1 \rangle_{Al8Mn5}$	0.239	0.264	10.5

directions; $\langle 111 \rangle_{Fe(Al)}$, $\langle 100 \rangle_{Fe(Al)}$, $\langle 110 \rangle_{Fe(Al)}$, and $\langle 113 \rangle_{Fe(Al)}$. The interatomic spacing along these four directions are

$$f = \frac{\sqrt{3}}{2}a_{Fe(Al)}$$

for $\langle 111 \rangle_{Fe(Al)}$, $f = a_{Fe(Al)}$ for $\langle 100 \rangle_{Fe(Al)}$, $f = \sqrt{2}a_{Fe(Al)}$ for $\langle 110 \rangle_{Fe(Al)}$ and $f = 0.25\sqrt{11}a_{Fe(Al)}$ for $\langle 113 \rangle_{Fe(Al)}$. Therefore, there will be sixteen direction pairs between Fe(Al) (BCC) and Al_8Mn_5 (rhombohedral) that can be potential matching directions. If we assumed that the Fe(Al) phase is the substrate and Al_8Mn_5 is the reaction product on the Fe(Al), the variation of interatomic spacing misfit along these direction pairs can be calculated. Table 3 shows the calculated results for the relative interatomic spacing misfits, δ, along possible matching directions between Fe(Al) and Al_8Mn_5.

To predict the ORs, the matching planes have also to be identified. In the BCC crystal structure, there are

Table 4 — Calculated Interplanar Spacing for Al_8Mn_5 Phase and Fe(Al) Substrate and Interplanar Spacing Mismatch between Possible Matching Planes of Al_8Mn_5 and Fe(Al)

Matching Planes	Fe(Al) Interplanar Spacing, nm	Al_8Mn_5 Interplanar Spacing, nm	Interplanar Mismatch
$\{110\}_{Fe(Al)}//\{30\bar{3}3\}_{Al8Mn5}$	0.204	0.221	8.3
$\{110\}_{Fe(Al)}//\{33\bar{6}0\}_{Al8Mn5}$	0.204	0.217	6.3
$\{200\}_{Fe(Al)}//\{30\bar{3}3\}_{Al8Mn5}$	0.144	0.221	53.5
$\{200\}_{Fe(Al)}//\{33\bar{6}0\}_{Al8Mn5}$	0.144	0.217	50.7
$\{111\}_{Fe(Al)}//\{30\bar{3}3\}_{Al8Mn5}$	0.166	0.221	33.1
$\{111\}_{Fe(Al)}//\{33\bar{6}0\}_{Al8Mn5}$	0.166	0.217	30.7

of 10% as the critical value for the interatomic spacing misfit is based on van der Merwe's energy calculation, which was done along the close-packed directions between face-centered cubic (FCC) and BCC (Ref.37). Similar to the interatomic spacing misfit along matching directions, it has been reported that the approximate critical *d* value mismatch to form an OR without large angle rotation of lattice planes is 6%. This is based on reported ORs in known systems (Ref. 38). The calculated data shown in Table 4 indicate that there is one plane pair with the interplanar spacing mismatch close to the critical value of 6%; $\{110\}_{Fe(Al)}//\{33\bar{6}0\}_{Al8Mn5}$ with 6.3% interplanar mismatch. This plane pair does not contain all the possible matching directions with small misfit values. It only contains three direction pairs, i.e., $\langle111\rangle_{Fe(Al)}//\langle11\bar{2}0\rangle_{Al8Mn5}$, $\langle111\rangle_{Fe(Al)}//\langle10\bar{1}1\rangle_{Al8Mn5}$, and $\langle110\rangle_{Fe(Al)}//\langle0001\rangle_{Al8Mn5}$. Therefore, combination of $\{110\}_{Fe(Al)}//\{33\bar{6}0\}_{Al8Mn5}$ plane pair and these direction pairs have the potential to form an OR. These conditions lead to a low-angle rotation of the lattice planes along the matching directions and a low mismatch strain at the interface of these two phases. Thus, the Fe(Al) phase can be regarded as an effective nucleating substrate for the Al_8Mn_5 phase. The plane pair of $\{110\}_{Fe(Al)}//\{30\bar{3}3\}_{Al8Mn5}$ might also have this potential to form an OR, but this would require a higher angle rotation of the matching planes. The HR-TEM experimental results in this study also showed that the OR at the interface between the Fe(Al) and Al_8Mn_5 was $[10\bar{1}1]_{Al8Mn5}//[1\bar{1}1]_{Fe(Al)}$, $\{110\}_{Fe(Al)}$ 4.2 deg from $\{30\bar{3}3\}_{Al8Mn5}$ with 5.2 % interplanar mismatch between them — Fig. 8A. Therefore, presented results in this study suggest that the Fe(Al) phase has small interatomic spacing misfit along the matching direction and very low *d*-value mismatch between the matching planes with Al_8Mn_5 phase. This leads to a low energy density and strong Fe(Al)-Al_8Mn_5 interface.

The edge-to-edge crystallographic

Table 5 — Interatomic Spacing Misfits along Possible Matching Directions between Mg Phase and Al$_8$Mn$_5$ Substrate

Matching Directions	Al$_8$Mn$_5$ Interatomic Spacing, nm	Mg Interatomic Spacing, nm	Interatomic Misfit (%)
$\langle11\bar{2}0\rangle_{Al8Mn5}//\langle11\bar{2}0\rangle_{Mg}$	0.244	0.320	31.1
$\langle11\bar{2}0\rangle_{Al8Mn5}//\langle10\bar{1}0\rangle_{Mg}$	0.244	0.277	13.5
$\langle11\bar{2}0\rangle_{Al8Mn5}//\langle11\bar{2}3\rangle_{Mg}$	0.244	0.305	25.0
$\langle1\bar{1}02\rangle_{Al8Mn5}//\langle11\bar{2}0\rangle_{Mg}$	0.289	0.320	10.7
$\langle1\bar{1}02\rangle_{Al8Mn5}//\langle10\bar{1}0\rangle_{Mg}$	0.289	0.277	4.2
$\langle1\bar{1}02\rangle_{Al8Mn5}//\langle11\bar{2}3\rangle_{Mg}$	0.289	0.305	5.5
$\langle0001\rangle_{Al8Mn5}//\langle11\bar{2}0\rangle_{Mg}$	0.401	0.320	20.2
$\langle0001\rangle_{Al8Mn5}//\langle10\bar{1}0\rangle_{Mg}$	0.401	0.277	30.9
$\langle0001\rangle_{Al8Mn5}//\langle1123\rangle_{Mg}$	0.401	0.305	23.9
$\langle10\bar{1}1\rangle_{Al8Mn5}//\langle11\bar{2}0\rangle_{Mg}$	0.264	0.320	21.1
$\langle10\bar{1}1\rangle_{Al8Mn5}//\langle10\bar{1}0\rangle_{Mg}$	0.264	0.277	4.9
$\langle10\bar{1}1\rangle_{Al8Mn5}//\langle11\bar{2}3\rangle_{Mg}$	0.264	0.305	15.5

Table 6 — Calculated Interplanar Spacing for Mg Phase and Al$_8$Mn$_5$ Substrate and Interplanar Spacing Mismatch between Possible Matching Planes of Mg and Al$_8$Mn$_5$

Matching Planes	Al$_8$Mn$_5$ Interplanar Spacing, nm	Mg Interplanar Spacing, nm	Interplanar Mismatch
$\{30\bar{3}3\}_{Al8Mn5}//\{0002\}_{Mg}$	0.221	0.260	17.6
$\{30\bar{3}3\}_{Al8Mn5}//\{10\bar{1}1\}_{Mg}$	0.221	0.244	10.4
$\{30\bar{3}3\}_{Al8Mn5}//\{10\bar{1}0\}_{Mg}$	0.221	0.277	25.3
$\{30\bar{6}0\}_{Al8Mn5}//\{0002\}_{Mg}$	0.217	0.260	19.8
$\{30\bar{6}0\}_{Al8Mn5}//\{10\bar{1}1\}_{Mg}$	0.217	0.244	12.4
$\{30\bar{6}0\}_{Al8Mn5}//\{10\bar{1}0\}_{Mg}$	0.217	0.277	27.6

matching model was also applied to the Al_8Mn_5-Mg interface. For Mg with a HCP crystal structure, there are three possible close-packed or nearly close-packed directions (directions with low indexes), i.e., $\langle11\bar{2}0\rangle_{Mg}$, $\langle10\bar{1}0\rangle_{Mg}$, and $\langle11\bar{2}3\rangle_{Mg}$. The interatomic spacing along these three potential matching directions can be expressed in terms of the lattice parameters, a_{Mg} and c_{Mg}. If *f* is used to represent interatomic spacing, then $f = a_{Mg}$ for $\langle11\bar{2}0\rangle_{Mg}$, $f = 0.5_{Mg}\sqrt{3}$ for $\langle10\bar{1}0\rangle_{Mg}$, and $f = 0.5(a_{Mg}^2 + c_{Mg}^2)^{0.5}$ for $\langle11\bar{2}3\rangle$. The lattice parameters of Mg used in the current study are a_{Mg} = 0.320 nm and c_{Mg} = 0.520 nm (Ref. 39). In the HCP crystal structure, the close-packed or nearly close-packed-planes are {0002}, {1011}, and {1010} with *d*-spacings of $c_{Mg}/2$,

$$\frac{a_{Mg}c_{Mg}\sqrt{3}}{\sqrt{4c_{Mg}^2 - 3a_{Mg}^2}} \ ,$$

and $\sqrt{3}a_{Mg}/2$, respectively.

If it is assumed that during cooling, the Mg (HCP) nucleates and grows onto the preexisting Al_8Mn_5 surface layer, the variation of interatomic spacing misfit along twelve possible close-packed or nearly close-packed directions pairs and also the variation of interplanar spacing mismatch along six possible close-packed or nearly close-packed plane pairs between Mg phase and Al_8Mn_5 substrate can be calculated (Tables 5, 6). If 10% is selected as the critical value of the interatomic spacing misfit, then three direction pairs satisfy this condition; $\langle1\bar{1}02\rangle_{Al8Mn5}//\langle10\bar{1}0\rangle_{Mg}$, $\langle1\bar{1}02\rangle_{Al8Mn5}//\langle11\bar{2}3\rangle_{Mg}$, and $\langle10\bar{1}1\rangle_{Al8Mn5}//\langle10\bar{1}0\rangle_{Mg}$. However, Zhang et al. (Ref. 36) reported that the first two direction pairs are combinations of straight Al_8Mn_5 atom rows and nonstraight Mg atoms rows and as a result they cannot be matched.

Therefore, the direction pair of $\langle10\bar{1}1\rangle_{Al8Mn5}//\langle10\bar{1}0\rangle_{Mg}$ is the only possible matched pair with interatomic

spacing misfit less than 10%. This direction pair involves two plane pairs, i.e., $\{30\bar{3}3\}_{Al8Mn5}//\{0002\}_{Mg}$ with 17.6% d-value mismatch and $\{3\bar{3}60\}_{Al8Mn5}//\{0002\}_{Mg}$ with 19.8% d-value mismatch (Table 6). Again, if 6% is used as the critical data of the d-value mismatch (Ref. 38), in both cases the d-value mismatches are much larger than the critical value. Therefore, the formed OR between Al_8Mn_5 and Mg will have a large angle rotation of the matching planes — Fig. 8B. Qui et al. (Ref. 40) also reported that Al_8Mn_5 has a high interplanar mismatch energy against α-Mg. Therefore, the formed Al_8Mn_5 phase cannot act as an effective site for heterogeneous nucleation and growth of the Mg from the molten FZ. Zhang et al. (Ref. 36) reported that the metastable τ-AlMn phase possesses significantly better crystallographic matching with the Mg matrix than the other Al-Mn intermetallic phases, such as $Al_8(Mn,Fe)_5$ phase.

Porosity Formation at the Steel-FZ Interface

In Figs. 5 and 6, there is evidence of a band of spherical, nanoscale pores that have formed parallel to the interface and within the single-phase Fe(Al) surface layer that was created during the laser brazing operation. This type of porosity is very similar to the Kirkendall porosity observed by Saiz et al. (Ref. 41) within a layer of $FeSn_2$ which formed parallel to the interface during soldering of a Fe-Ni alloy using Sn-Ag solder at 523 K (250ºC). Salamon and Mehrer (Ref. 42) have observed Kirkendall porosity formation in the diffusion zone of a $Fe_{82}Al_{18}/Fe_{58}Al_{42}$ diffusion couple. Springer et al. (Ref. 43) reported formation of Kirkendall porosity in the reaction layer Fe_2Al_5 formed at the interface of friction stir welded steel to Al alloy joints. Finally, Tiwari and Mehrotra (Ref. 44) have observed Kirkendall effect and Kirkendall porosity in their recent study of interphase interdiffusion mechanisms in NiAl and FeAl intermetallic compounds.

The necessary condition for occurrence of Kirkendall effect and formation of Kirkendall porosity in a binary diffusion couple is that two diffusing species should have unequal intrinsic diffusion coefficients (Ref. 42). In the present study, considering the location of the porosity (Fig. 6), the Kirkendall porosity is formed during inter-diffusion of the Al and Fe atoms within the Fe-Al diffusion layer; however, since the diffusivity of Al in Fe is greater than Fe in Al, there is a net flux of vacancies in the opposite direction of the Al diffusion that results in vacancy concentrations that exceed equilibrium values and ultimately result in nucleation and growth of nanopores similar to those shown in Figs. 5 and 6 (Refs. 42, 44, 45).

In Figs. 5 and 6, the average area fraction of Kirkendall porosity in the shear plane parallel to the interface is about 15%. However, this reduction in throat area due to the porosity was not sufficient to compromise the strength of the interface, primarily because of the significant strength of the Fe(Al) layer relative to the steel and the Mg-Al-Zn brazing alloy. The ultimate tensile strength (UTS) of Fe(Al) along the [001] crystallographic direction has been reported to be 19,000 MPa (Ref. 46), whereas the UTS for the steel sheet was 344 MPa and the Mg-Al-Zn brazing alloy was 170 MPa (Ref. 47). Thus, even with the Kirkendall porosity defects, the strength of the Fe(Al) layer far exceeds the strength of the steel and Mg-Al-Zn brazing alloy so that the Kirkendall porosity did not limit the overall tensile shear strength of the joint.

Sequence of Phase Formation along the Interface (Bonding Mechanism)

Based on the results described above, a sequence of events may be surmised to take place during laser brazing of the Sn-plated steel and the AZ31B Mg sheet. These are shown in the schematics in Fig. 9 starting with the original joint configuration at room temperature shown in Fig. 9A. During initial heating (Fig. 9B), the electroplated Sn layer melts when the temperature exceeds the melting temperature of the Sn (505 K [232ºC]). At this stage, the steel surface is still covered by $Sn_{(l)}$, which continues to pre-

vent oxidation of the steel surface. As shown in Fig. 9C, at higher temperatures approaching 873 K (600 ºC), the flux is activated and then melting of the Mg-Al-Zn brazing alloy begins. The liquid Sn layer then easily diffuses from the interface into the molten FZ (Fig. 9C), thereby allowing direct contact between the molten filler metal and the clean, oxide-free steel surface. At this stage, Al atoms from the fusion zone preferentially diffuse very rapidly from the molten FZ into the steel leading to the formation of a Fe(Al) diffusion layer — Fig. 9D.

Continued diffusion of the Al into the steel and growth of the Fe(Al) layer result in the formation of nanosized Kirkendall pores within the Fe(Al) diffusion layer. As shown in Fig. 9E, as cooling and solidification begins, the newly formed Fe(Al) layer also acts as an effective site for heterogeneous nucleation and growth of the Al_8Mn_5 phase from the molten FZ. The good OR and lattice matching that exist between the Al_8Mn_5 and Fe(Al) phases result in low interfacial energy density and good bonding between these two phases along the fusion zone-Fe(Al) interface. Meanwhile, some Fe atoms from the substrate diffuse into this newly formed Al_8Mn_5 interfacial phase. As the temperature continues to drop, this $Al_8(Mn,Fe)_5$ intermetallic compound with rhombohedral crystal structure provides a surface for heterogeneous nucleation and growth of the solid α-Mg phase from the molten FZ. Finally, continued cooling and solidification of the FZ result in an equiaxed dendritic mixture of primary α-Mg and α-Mg + $Mg_{17}Al_{12}$ eutectic phases — Fig. 9E.

It is interesting to note that the Sn coating on the steel does not appear to play a role in creating the final bond between the Mg-Al-Zn brazing alloy and the steel sheet. However, the Sn coating layer was essential to prevent oxidation of the steel surface during initial heating and prior to activation of the flux and direct contact between the molten filler alloy and the steel surface. Dissolution of the molten Sn layer into the molten fusion zone allows a clean and oxide-free steel surface to come in direct contact with the molten filler metal. Similar functional behavior for the interlayer was recently reported by Wahba and

Katayama (Ref. 48) in laser welding of AZ31B magnesium alloy to Zn-coated steel, where Zn played the role of the interlayer.

Conclusions

It has been shown that diode laser brazing can be successfully performed between 2-mm-thick AZ31B-H24 Mg alloy sheet and 0.6-mm-thick Sn-coated plain carbon steel sheet in the lap joint configuration using a Mg-Al-Zn brazing alloy wire.

In all cases, tensile shear tests failed in the steel sheet indicating that the Mg-Al-Zn brazing alloy-to-steel sheet interface and braze joint were always stronger than the steel sheet.

The formation of nano-scale layers of Fe(Al) solid solution and $Al_8(Mn,Fe)_5$ intermetallic compound was found to be responsible for the formation of a metallurgical bond between the steel and Mg-Al-Zn brazing alloy.

HR-TEM analysis of the Fe(Al)-Al_8Mn_5 interface showed that a crystallographic orientation relationship with low angle rotation of the matching planes and low interplanar mismatch existed at the Fe(Al)-Al_8Mn_5 interface. However, Al_8Mn_5-Mg interface showed a poor crystallographic matching between Al_8Mn_5 and α-Mg with a large angle rotation of matching planes at their interface.

These results were further confirmed by the predictions of an edge-to-edge crystallographic matching model of the Fe(Al)-Al_8Mn_5 and Al_8Mn_5-Mg interfaces. These conditions will result in an interface with low interfacial energy density and strong metallic bond between the Fe(Al) and the Al_8Mn_5 and an interface with high interfacial energy density and weak bond between the Al_8Mn_5 and the Mg in the filler metal.

The Sn coating on the steel sheet does not appear to contribute to the final metallic bonding of the steel to the AZ92 filler metal. Instead, its primary role is to prevent contamination and oxidation of the steel surface until molten Mg-Al-Zn brazing alloy can come into direct contact with the steel surface.

References

1. Cole, G. S. 2003. Issues that influence magnesium's use in the automotive industry. *Materials Science Forum* 419: 43–50.

2. Watarai, H. 2006. Trend of research and development for magnesium alloys-reducing the weight of structural materials in motor vehicles. *Science & Technology Trends - Quarterly Review* 18: 84–97.

3. Jana, S., and Hovanski, S. 2012. Fatigue behaviour of magnesium to steel dissimilar friction stir lap joints. *Science and Technology of Welding and Joining* 17: 141–145.

4. Liu, L. 2005. *Welding and Joining of Magnesium Alloys*. Cambridge, Woodhead Publishing Ltd.

5. Miao, Y. G., Han, D. F., Yao, J. Z., and Li, F. 2010. Microstructure and interface characterization of laser penetration brazed magnesium alloy and steel. *Science and Technology of Welding and Joining* 15: 97–103.

6. Liu, L., Xiao, L., Feng, J., Li, L., Esmaeili, S., and Zhou, Y. 2011. Bonding of immiscible Mg and Fe by coated nanoscale Fe_2Al_5 transition layer. *Scripta Materialia* 65: 982–985.

7. Liu, L., and Qi, X. 2010. Strengthening effect of nickel and copper interlayers on hybrid laser-TIG welded between magnesium alloy and mild steel. *Materials & Design* 31: 3960–3963.

8. Li, L., Tan, C., Chen, Y., Guo, W., and Hu, X. 2012. Influence of Zn coating on interfacial reactions and mechanical properties during laser welding-brazing of Mg to steel. *Metallurgical and Materials Transactions* A 43: 4740-4754.

9. Zhao, X., Song, G., and Liu, L. 2006. Microstructure of dissimilar metal joint with magnesium alloy AZ31B and steel 304 for laser-tungsten inert gas lap welding. *Transactions of China Welding Institution* 27: 56–62.

10. Liu, L., Xiao, L., Feng, J. C., Tian, Y. H., Zhou, S. Q., and Zhou, Y. 2010. The mechanism of resistance spot welding of magnesium to steel. *Metallurgical and Materials Transactions* A 41: 2651–2661.

11. Liu, L. M., and Qi, X. 2009. Effects of copper addition on microstructure and strength of the hybrid laser-TIG welded joints between magnesium alloy and mild steel. *Journal of Materials Science* 44: 5725–5731.

12. Liyange, T., Kilbourne, J., and Gerlich, A. P. 2009. Joint formation in dissimilar Al alloy/steel and Mg alloy/steel friction stir spot welds. *Science and Technology of Welding and Joining* 14: 500–508.

13. Jana, S., Hovanski, Y., and Grant, G. J. 2010. Friction stir lap welding of magnesium alloy to steel: A preliminary investigation. *Metallurgical and Materials Transactions* A 41: 3173–3182.

14. Nasiri, A. M., Li, L., Kim, S. H., Zhou, Y., Weckman, D. C., and Nguyen, T. C. 2011. Microstructure and properties of laser brazed magnesium to coated steel. *Welding Journal* 90(1): 211-s to 219-s.

15. Nasiri, A. M., Weckman, D. C., and Zhou, Y. 2013. Interfacial microstructure of diode laser brazed AZ31B magnesium to steel sheet using a nickel interlayer. *Welding Journal* 92(1): 1-s to 10-s.

16. Tan, C. W., Chen, Y. B., Li, L. Q., and Guo, W. 2013. Comparative study of microstructure and mechanical properties of laser welded-brazed Mg/steel joints with four different coating surfaces. *Science and Technology of Welding and Joining* 18: 466–472.

17. Li, L., Tan, C., Chen, Y., Guo, W., and Mei, C. 2013. CO_2 laser welding-brazing characteristics of dissimilar metals AZ31B Mg alloy to Zn coated dual phase steel with Mg based filler. *Journal of Materials Processing Technology* 213: 361–375.

18. Li, L., Tan, C., Chen, Y., Guo, W., and Song, F. 2013. Comparative study of microstructure and mechanical properties of laser welded-brazed Mg/mild steel and Mg/stainless steel joints. *Materials & Design* 43: 59–65.

19. Sierral, G., Peyre, P., Deschaux Beaume, F., Stuart, D., and Fras, G. 2008. Steel to aluminum braze welding by laser process with Al-12Si filler wire. *Science and Technology of Welding and Joining* 3: 430–437.

20. Lockwood, L., and Shapiro, A. E. 2005. Brazing of Magnesium. *Brazing Handbook*. 5th edn., American Welding Society, Miami, Fla.

21. Kreimeyer, M., Wagner, F., and Vollertsen, F. 2005. Laser processing of aluminum-titanium-tailored blanks. *Optics and Lasers in Engineering* 43: 1021–1035.

22. Material Safety Data Sheet. 2003. Flux No. 21, Superior Flux & Mfg. Co. Cleveland, Ohio, *www.superiorflux. com/superior_flux_msds_spec_sheets.html*

23. Saida, K., Song, W., and Nishimoto, K. 2005. Diode laser brazing of aluminum alloy to steels with aluminum filler metal. *Science and Technology of Welding and Joining* 10: 227–235.

24. Vander Voort, G. F. 1999. *Metallography Principles and Practice*. ASM International, Materials Park, Ohio.

25. Schwartz, M. M. 1987. *Brazing*. ASM International, Materials Park, Ohio.

26. *ASM Handbook*. 1994. Alloy Phase Diagrams. 10th ed. ASM International, Materials Park, Ohio.

27. Potesser, M., Schoeberl, T., Antrekowitsch, H., and Bruckner, J. 2006. The characterization of the intermetallic Fe-Al layer of steel-aluminum welding. *Proceeding of EPD Congress*, Howard S. M. et al. eds. TMS (The Minerals, Metals & Materials Society), Warrendale. Pa.

28. Kogachi, M., and Haraguchi, T. 1997. Quenched-in vacancies in B2-structured intermetallic compound FeAl. *Materials Science and Engineering* A 230: 124–131.

29. Kim, Y. M., Yim, C. D., and You, B. S. 2007. Grain refining mechanism in Mg-Al alloys with carbon addition. *Scripta Materialia* 57: 691–694.

30. Xiao, L., Liu, L., Esmaeili, S., and Zhou, Y. 2012. Microstructure refinement after the addition of titanium particles in the AZ31 magnesium alloy resistance spot welds. *Metallurgical and Materials Transactions* A 43: 598–609.

31. Freund, L. B., and Suresh, S. 2003. *Thin Film Materials, Stress, Defect Formation and Surface Evolution*. Cambridge, University Press.

32. Turnbull, D., and Vonnegut, R. 1952. *Nucleation Catalysis. Industrial & Engineering Chemistry* 44: 1292–1298.

33. Zhang, M. X., and Kelly, P. M. 2005. Edge-to-edge matching and its applications: Part I — Application to the simple HCP/BCC system. *Acta Materialia* 53: 1073–1084.

34. Zhang, M. X., and Kelly, P. M. 2005. Edge-to-edge matching and its applications: Part II — Application to Mg–Al, Mg–Y and Mg–Mn alloys. *Acta Materialia* 53: 1085–1096.

35. Villars, P., and Calvert, L. D. 1991. *Pearson's Handbook of Crystallographic Data for Intermetallic Phases*. ASM International, Materials Park, Ohio.

36 Zhang, M. X., Kelly, P. M., and Qian, M. 2005. Crystallography of grain refinement in Mg-Al based alloys. *Acta Materialia* 53: 3261–3270.

37. van der Merwe, J. H. 1982. Analytical selection of ideal epitaxial configurations and some speculations on the occurrence of epitaxy. *Philosophical Magazine* A 45: 127–143, 145–157, and 159–170.

38. Duly, D. 1993. Application of the invariant line model for b.c.c./h.c.p. couples: A criterion based on surface variations. *Acta Metallurgica et Materialia* 41: 1559–1566.

39. Pearson, W. B. 1958. *Lattice Spacings and Structures of Metals and Alloys*. New York, Pergamon Press.

40. Qiu, D., Zhang, M. X., Taylor, J. A., Fu, H. M., and Kelly, P. M. 2007. A novel approach to the mechanism for the grain refining effect of melt superheating of Mg–Al alloys. *Acta Materialia* 55: 1863–1871.

41. Saiz, E., Hwang, C. W., Suganuma, K., and Tomsia, A. P. 2003. Spreading of Sn-Ag solders on FeNi alloys. *Acta Materialia* 51: 3185–3197.

42. Salamon, M., and Mehrer, H. 2005. Interdiffusion, Kirkendall effect, and Al self-diffusion in iron–aluminium alloys. *Zeitschrift für Metallkunde* 96: 4–16.

43. Springer, H., Kostka, A., dos Santos, J. F., and Raabe, D. 2011. Influence of intermetallic phases and Kirkendall-porosity on the mechanical properties of joints between steel and aluminium alloys. *Materials Science and Engineering* A 528: 4630–4642.

44. Tiwari, G. P., and Mehrotra, R. S. 2012. Kirkendall effect and mechanism of self-diffusion in B2 intermetallic compounds. *Metallurgical and Materials Transactions* A 43: 3654–3662.

45. Borg, R. J., and Dienes, G. J. 1988. *An Introduction to Solid State Diffusion*. Boston, Academic Press, Inc.

46. Li, T., Morris, J. W., and Chrzan, D. C. 2004. Ideal tensile strength of B2 transition-metal aluminides. *Physical Review* B 70: 054107.

47. Avedesian, M. M., and Bake, H. 1999. *Magnesium and Magnesium Alloys*. ASM International, Materials Park, Ohio.

48 Wahba, M., and Katayama, S. 2012. Laser welding of AZ31B magnesium alloy to Zn-coated steel. *Materials & Design* 35: 701–706.

CAN WE TALK?